Plasma Sources Sci. Technol. 3 (1994) 190–205. Printed in the UK

Ion energy distributions in radio frequency discharges sustained in gas mixtures obtained using a Monte Carlo–fluid hybrid model: endothermic processes and ion Holes

Helen H Hwang and Mark J Kushner

University of Illinois, Department of Electrical and Computer Engineering, 1406 W. Green Street, Urbana, IL 61801, USA

Received 2 August 1993, in final form 5 November 1993

Abstract. The distributions of ion energies striking the substrate in radio frequency (RF) discharges are important with respect to the use of these devices for the etching of semiconductors and the fabrication of microelectronic devices. Previous works have demonstrated the importance of symmetric charge exchange and elastic collisions in the sheath in thermalizing the ion energy distributions (IEDs) and spreading their angular distribution. These processes have essentially gas kinetic rates since they have no activation energy. Ions can, however, be accelerated in the sheaths to energies above the threshold for non-thermal charge exchange collisions. These endothermic processes can result in a significant perturbation of the IEDs and ion mixing. In this work, we investigate the consequences of non-thermal charge exchange processes in parallel plate RF discharges using a Monte Carlo–fluid hybrid model. In this model particle simulations are used to resolve electron and ion energy distributions, while a fluid model is used to obtain species densities and electric fields. The reactor geometry is based on the GEC Reference Cell and we simulate both symmetric and asymmetric discharges. The gas mixtures we have investigated are pure argon, He/N_2, and $He/CF_4/H_2$. Ion energy distributions are presented which show depletion at energies greater than the threshold for endothermic processes. To account for particle–mesh interactions in the hybrid model a new technique called 'ion holes' is used in the particle simulation. Ion holes account for the dual loss of pseudoparticles resulting from, for example, ion–ion neutralization collisions, and remove trajectories from phase space resulting from the loss of a fluid ion.

1. Introduction

The anisotropic etching of semiconductor materials which one obtains in low-pressure radio frequency (RF) glow discharges is largely a result of vertically directed energetic ion bombardment of the wafer. Energy delivered to the wafer by these ions preferentially activates etching on horizontal surfaces on the bottom of trenches, as opposed to the vertical walls of trenches. The ion energy distributions (IEDs) and ion angular distributions (IADs) are therefore of great interest in optimizing the etching process. Recently, hot neutral atoms and molecules, produced by either charge exchange reactions of energetic ions or by gas phase dissociation processes, have been studied. Hot neutrals may be as efficient in activating surface processes as ions, and therefore their energy and angular distributions are of equal importance. For example, Maneschijn and Goedheer [1] modelled ion and hot atom transport in the sheaths of argon RF discharges. They found the angular distribution of the hot neutrals to be quite broad compared with ions, while the ranges of their energy distributions were commensurate with those of ions.

A number of previous works have experimentally and theoretically characterized IEDs and IADs in RF discharges with the goal of predicting etching profiles. These works have clearly shown the importance of both charge exchange and elastic collisions of ions in the sheaths with respect to shaping the IED and IAD. Using a Monte Carlo simulation, Kushner [2] correlated thermalization of the IED and the broadening of the IAD with the degree of collisionality in the sheath. Thompson *et al* [3] also used a Monte Carlo simulation to track ion trajectories through the sheath and examined the effects of the type of ion–molecule scattering and the mass of the collision partner. They found that lighter ions, which have more backscattering elastic collisions, experience more net collisions in the sheaths than do heavy ions which predominantly scatter in the forward direction. The mean energy of the heavier ions, for otherwise

0963-0252/94/020190 + 16 $19.50

identical conditions, is therefore somewhat larger. Liu *et al* [4] later measured IEDs and IADs in a parallel plate RF discharge sustained in Ar. Their measurements showed that the transition between a largely collisionless sheath and a collisional sheath occurred between 10 and 50 mTorr. At lower pressures, more energetic ions arrive at shallower angles, whereas at higher pressures, the dependence of the IED on angle was weak. These results corroborate the measurements of Ingram and Braithwaite [5] who determined that the onset of collisional scattering in the sheath of an Ar RF discharge occurs at $\simeq$40 mTorr. Manenschijn and Goedheer [1] found this transition to occur at 10–20 mTorr for Ar ions striking the powered electrode.

The general conclusions of these and other works are that increasing rates of charge exchange collisions resulting from operating at high gas pressures both decrease the average energy of ions striking the substrate and broaden their angular spread. Elastic collisions are less efficient at reducing ion energies, but are equally important at broadening the IAD. Under collisionsless conditions, the IED can be characterized by a parameter $s = \Delta t_c/\Delta t_{RF}$, where Δt_c is the crossing time of an ion through the sheath, and Δt_{RF} is the RF period. When $s \ll 1$, the ion can cross the sheath in a time that is short compared with the RF cycle, and therefore strikes the electrode with the full instantaneous sheath potential. When $s \gg 1$, the ion experiences an average sheath potential and the IED has a single peak centred on that value.

Only a few previous works on IEDs in RF discharges have addressed mixed gases. Kuypers and Hopman [6] investigated IEDs in Ar/H_2 mixtures at fairly low pressures (3 mTorr) where charge exchange in the sheaths is not believed to be important. They were able to distinguish clearly between the contributions of Ar^+, H_2^+, and H_3^+ ions in the IEDs. The large abundance of H_3^+ that is observed results from the exothermic charge exchange reaction $H_2^+ + H_2 \rightarrow H_3^+ + H$ in the bulk plasma. As a result H_2^+, which is the most abundant product of electron impact ionization of H_2, may not survive to reach the substrate in large numbers. Using analytic expressions for the sheath potential and thickness, Manenschijn *et al* [7] simulated these multicomponent IEDs to confirm the cited identifications. The resulting distributions revealed Ar^+ (or ArH^+), H_2^+, and H_3^+ as the dominant ions striking the electrode. The difference between the energy peaks of the bimodal distributions varied inversely with the square root of ion mass, an effect also shown by the results of Kuypers and Hopman [6]. Field *et al* [8] performed a similar analysis for Ar, Ar/H_2, CF_4, and O_2 gas mixtures.

In multicomponent gas mixtures, charge exchange collisions between different ion species can complicate the interpretation of experiments and the prediction of optimum reactor conditions. These ion molecule reactions come in at least two varieties: exothermic reactions and endothermic reactions. In our context, endothermic reactions have threshold energies greater than a few tenths of an eV, and are characteristic of the thermal or epithermal energies of ions in the bulk plasma. The importance of exothermic ion–molecule reactions in both single and multicomponent gas mixtures has been recognized by a number of workers. One example is the large abundances of H_3^+ observed in the Ar/H_2 discharges discussed above. Another example comes from the work of Toyada *et al* [9] who measured the abundance of CH_n^+ ions in an RF discharge sustained in methane at pressures of 0.5–20 mTorr. The electron impact ionization of CH_4 produces CH_4^+ and CH_3^+ in the greatest abundances. Toyada *et al* found, however, that at pressures >1 mTorr, CH_5^+ and $C_2H_5^+$ are the dominant ions which strike the electrodes. These are products of exothermic charge exchange of CH_4^+ and CH_3^+ with CH_4.

The contributions of endothermic ion–molecule reactions and non-symmetric charge exchange to ion fluxes in RF discharges have not been previously examined in detail. These reactions can have important repercussions on the final identity and energy of the ions which strike the substrate. The importance of endothermic charge exchange reactions in Townsend discharges, and a compilation of cross sections, have recently been presented by Phelps [10, 11]. Cross sections for a variety of endothermic charge exchange reactions for systems of interest to plasma processing have been measured by Armentrout and co-workers [12–19]. For example, CF_4/O_2 mixtures are often used to obtain selectivity in etching of Si over SiO_2. The ionization potential of O_2^+ is 12.07 eV while the thermodynamic appearance potentials of $CF_3^+ (+ F)$ and $CF_2^+ (+ 2F)$ from CF_4 are 14.2 and 20.6 eV respectively. Charge exchange reactions of O_2^+ with CF_4 in the bulk plasma are therefore endothermic by 2.2 and 8.5 eV for branching to these products. Fisher and Armentrout [12] measured cross sections for these processes and found threshold energies of 3.6 eV and 10.6 eV respectively, slightly higher than the thermodynamic values. For example, the cross section for producing CF_3^+ from charge exchange between O_2^+ and CF_4 has a maximum value of 3×10^{-16} cm^2 at $\simeq$20 eV. This result implies that in the bulk plasma of a CF_4/O_2 RF discharge, O_2^+ undergoes only elastic collisions with CF_4. When accelerated to >10 eV in the sheaths, O_2^+ will charge exchange with CF_4. The mean free path for O_2^+ to charge exchange with CF_4 at energies >10 eV is 0.1 Torr cm. O_2^+ is therefore inelastically collisional with CF_4 in the sheath at partial pressures of greater than a few hundred mTorr. These interactions will significantly alter both the identity of the ions which strike the electrode and the shape of the IED.

To date, the ion dynamics of RF discharges in multicomponent gas mixtures in the regime where charge exchange and endothermic processes in the sheaths are important (pressures >20–40 mTorr) has not been theoretically investigated. To address these conditions, we have developed a Monte Carlo–fluid hybrid (MCFH) model for RF discharges with which non-equilibrium ion transport and endothermic ion–molecule reactions may be studied. The model combines a Monte Carlo simulation for the non-equilibrium transport of electrons and

ions with a fluid model for total charge densities and electric fields. This hybrid technique has proved to be quite versatile in modelling a variety of complex gas chemistries [20]. In principle, any reasonable number of species and complexity of reaction schemes may be addressed with this model. Limitations are largely due to the availability of cross sections and rate coefficients.

We find that at intermediate pressures ($\approx$100 mTorr), inelastic processes can dominate the IED since the ions are more energetic in the sheaths and can access endothermic collisions which have high threshold energies. The resulting IEDs are 'cut off' at the inelastic threshold in a similar fashion as observed for electron energy distributions in gases with low vibrational excitation or electronic excitation energy thresholds. Ions which undergo non-thermal charge exchange are depleted relative to other ions in the mixture. Conversely, ions which have higher ionization potentials (and are the products of the endothermic reactions) strike the electrode with greater abundance due to these processes. In section 2 we will describe the ion/electron MCFH model, followed by a discussion of ion dynamics in Ar, He/N_2, and $He/CF_4/H_2$ gas mixtures in section 3. Our concluding remarks are in section 4.

2. Description of the model

The model used in this study is a self-consistent Monte Carlo–fluid hybrid (MCFH) model for the electron, ion, and neutral kinetics in parallel plate RF discharges. The MCFH model consists of four linked simulations: an electron Monte Carlo simulation (EMCS), an ion Monte Carlo simulation (IMCS), a self-consistent fluid model (SCFM), and a neutral chemistry and transport model (NCTM). The MCFH model, composed of only the EMCS, SCFM, and NCTM, has been previously discussed in detail [20,21] and therefore will be only briefly described here. The addition of the IMCS will be discussed in detail following that description.

2.1. Description of the electron MCS and fluid models

The MCFH uses the EMCS to generate non-equilibrium electron impact source functions and transport coefficients as a function of position and phase (z, φ) in the RF cycle. These values are then used in the SCFM in which Poisson's equation is solved to obtain charge densities and electric fields as a function of (z, φ). These values are sent back to the EMCS, and the process is iterated until convergence. In the EMCS, electron trajectories are calculated in an oscillating RF electric field while accounting for collisions with the input gases, ions, and other species which evolve during the simulation. The EMCS begins by assuming an electric field as a function of position between the electrodes and phase during the RF cycle, $E(z, \varphi)$. This electric field is used to advance the electron trajectories for tens of RF cycles to generate electron impact source functions, $S(z, \varphi)$, for excitation, ionization, and dissociation of the gases as a function of position and phase. Electron transport coefficients (mobility, average energy) are also produced in the EMCS. The $S(z, \varphi)$ and transport coefficients are then transferred to the SCFM. In the SCFM the charge densities for electrons, positive ions and negative ions are obtained from their respective continuity equations using the source functions and transport coefficients from the EMCS. $E(z, \varphi)$ is obtained in the SCFM by solving Poisson's equation. All pertinent reactions of heavy charged particles (e.g. Penning ionization and charge exchange) are included in this portion of the model. The SCFM is also run for tens of RF cycles. At this time, the charge densities and $E(z, \varphi)$ are returned to the EMCS. The EMCS is run for tens of RF cycles using the new fields, generating new source functions for use in a subsequent run of the SCFM. We continue iterating between the EMCS and SCFM until the average plasma density converges to acceptable limits.

Before execution of the SCFM during each iteration, $S(z, \varphi)$ and the charge densities may be transferred to the NCTM model in which neutral radical and molecular densities are calculated. The resulting densities are then used in both the EMCS and SCFM. Modified null cross section techniques [20, 22] are extensively used to account for time and spatially varying densities of collision partners for electron and ion particles (see below). Typically, hundreds to thousands of RF cycles are required for the calculation to converge. This requires hours to tens of hours on a laboratory computer (Kubota 3000).

2.2. Description of the ion MCS

In previous works [20,21] no kinetic information was obtained for the IEDs since ion transport was included only in the SCFM. In this work we have added an IMCS which is run in parallel with the EMCS. The execution of the IMCS is conceptually similar to that of the EMCS. The $E(z, \varphi)$ obtained from the SCFM is used to advance the trajectories of positive and negative ion pseudoparticles in the IMCS in the same manner as in the EMCS. Trajectories for ion pseudoparticles are initialized at the (z, φ) corresponding to electron impact ionization and attachment collisions during the EMCS, and heavy particle collisions in the IMCS. The IMCS accounts for collisions of positive and negative ions with feedstock gases (elastic, charge exchange, detachment), radicals (elastic and charge exchange), other ions (elastic and ion–ion neutralization), and electrons (recombination) using the modified null cross section technique developed for electron transport [22]. Where appropriate, the energy dependence of the cross sections is included, as described below.

Collisions of electron and ion pseudoparticles with species which are generated during the simulation (i.e. radicals, dissociation products, ions) are accounted for using a modified null cross section. The use of the modified null cross section technique has been described in detail in the literature [20,22], but will be briefly discussed here. When initially computing the collision

frequencies for use in the EMCS and IMCS, an estimate of the maximum density of non-feedstock species, N_{mi}, is made. The total collision frequency of an electron or ion at a given speed v is then

$$\nu(v) = \sum_i v\sigma_i N_{mi} + \nu_n(v) \tag{1}$$

where σ_i is the cross section for collisions with species i. (More than one type of collision per species is allowed, but for simplicity the second index is suppressed here.) ν_n is the null collision frequency which accounts for variations in the total collision frequency as a function of particle energy. When a non-null collision of the pseudoparticle occurs in the MCS, the identity of the collision is obtained from selecting a random number $r = [0, 1]$ and finding the process which satisfies

$$P_{i-1} \leqslant r \leqslant P_i \qquad P_i = \frac{\Sigma_{j=1,i} v\sigma_i N_{im}}{\nu(v)} \tag{2}$$

where P_i is the cumulative probability for process i. This procedure selects a particular collision based on estimated bounds for the densities of the collision partners. To determine if the selected collision is real, an additional random number is chosen and compared with the instantaneous local density of species i, or $N_i(z, \varphi)$. If

$$r \leqslant \frac{N_i(z, \varphi)}{N_{im}} \tag{3}$$

then a real collision occurs. If the inequality does not hold, then the collision is considered null.

The collision partners for ion pseudoparticles include neutral radicals, product neutrals, and ions in addition to feedstock gases. Collisions with electron and ion pseudoparticles can also be included as these species evolve during the simulation. For example, ion densities which are obtained from the SCFM can be included in the collision probabilities (equation (1)) for ion pseudoparticles to account for electron–ion recombination, electron–ion detachment collisions, and ion–ion neutralization collisions. Collisions of electron and ion pseudoparticles with all other species which are accounted for in the manner described above are particle–mesh or particle–fluid interactions since the pseudoparticles are colliding with the continuum background fluid through which they move. As a result of particle–fluid collisions, the number or identity of pseudoparticles can change.

The following types of collisions, which change the number of electron or ion pseudoparticles, can be easily implemented when collisions are particle–fluid interactions.

(a) Electron impact ionization: electron and positive ion pseudoparticles are launched at the location of the ionization.

(b) Electron impact attachment: an electron pseudoparticle is removed and a negative ion pseudoparticle is launched.

(c) Ion–neutral collision producing one or more product ions: the identity of the ion pseudoparticle is changed and its velocity is updated. If necessary, a second ion pseudoparticle is initialized.

Collisions of electron or ion pseudoparticles with the ion fluids are possible, although problematic. For example, in a recombination collision between an electron pseudoparticle and positive ion fluid, the electron particle is easily removed. Similarly for an ion–ion neutralization collision between a negative ion pseudoparticle and positive ion fluid, the negative ion particle is also easily removed. Accounting for the postive ion which is lost in both of these processes is less straightforward. The loss of ions from the ion–fluid from this collision negatively contributes to the source function for that species which is transferred to the SCFM during the next iteration. One must, however, also include an appropriate loss of ion pseudoparticles to account for the consequences of the collision on the IED properly.

One method to deplete the ion pseudoparticles is to search for an appropriate ion pseudoparticle in the vicinity of the collision and remove it. This is a statistically poor method because there is no guarantee that there will be a pseudoparticle ion of the proper species at an acceptably close (z, φ). A second method is to use ion holes, which is explained below.

2.3. Ion holes

In our MCSs, pseudoparticles are assigned a 'weight' w_i. The weight denotes how many real electrons or ions each pseudoparticle represents. The weight of the pseudoparticle is used in collecting statistics on the particle distribution function. For example, after every advance of a pseudoparticle's position using time step Δt terminating with energy ε, the particle distribution function at location (z, φ) is incremented by $\Delta f(\varepsilon, z, \varphi) = w_i \Delta t$. This weight may vary during the simulation as a result of ionizations and loss processes which change the number of pseudoparticles beyond acceptable bounds, thereby requiring renormalization of the number and weighting of the pseudoparticles.

If it was possible to use a sufficiently large number of ion pseudoparticles, there would be an ion pseudoparticle at the precise (z, φ) at which an ion removing collision with the ion fluid occurred. That ion pseudoparticle could then be removed from the simulation. This procedure is essentially a particle–particle interaction. In the context of this work, an unreasonably large number of ions would be required to invoke particle–particle interactions. We nevertheless need to remove a pseudoparticle ion trajectory in the (v, z, φ) phase space as a result of, for example, an ion–ion neutralization collision. With our weighting convention, this goal can be achieved in the following manner. When a collision of a pseudoparticle with an ion fluid results in the removal of a fluid ion, an ion pseudoparticle is launched with a *negative* weight. This negatively weighted ion, which we call an 'ion hole', serves somewhat the same function as do holes in semiconductor

transport. The ion hole denotes the absence of an ion following a particular trajectory in the (v, z, φ) phase space. The ion hole is functionally treated as a real ion pseudoparticle, and has the same mass, charge, and identity as a positively weighted pseudoparticle. Ion holes respond to the electric field (positively charged ion holes are accelerated by a positive electric field) and undergo collisions with the charged and neutral fluids in the same manner as do ion pseudoparticles. The ion holes are included in the collection of statistics by incrementing the particle distribution by $\Delta f(\varepsilon, z, \varphi) = w_i \Delta t$, which in the case of ion hole is negative. When an ion hole suffers a collision with the ion fluid which results in the removal of an ion in an ion–ion neutralization reaction, for example, a negatively weighted ion hole, or a positively weighted ion pseudoparticle, is launched. This accounting procedure is valid to successive generations of ion hole interactions.

2.4. Cross sections

For a few select systems, the energy dependence of ion–molecule reactions from thermal energies to tens to hundreds of eV is known. When available, these data have been used in the MCFH model. The energy dependencies of most of the ion–molecule reactions of interest, however, are not known. The vast majority of ion–molecule reactions for which data are available are characterized by a thermal reaction rate coefficient, usually obtained from drift tube data. This value can be easily converted to a cross section for use in the IMCS. In the bulk plasma, these thermal cross sections are sufficient since the ion energies do not typically exceed a few tenths of an eV. Near and in the sheath, the ion energies can exceed tens to hundreds of eV, and the energy dependencies of ion molecule reactions are necessary. A number of experimental and theoretical works have determined semi-analytic functional forms for the energy dependence of ion–molecule reactions. In the absence of energy-dependent experimental cross section data or other experimental data (or for the purpose of performing parametric studies), we have adopted the following conventions.

(a) Symmetric charge exchange cross sections are determined from the ion mobility by allocating ninety per cent of the momentum transfer cross section to charge change, and the remaining ten per cent to elastic collisions. All such collisions are assumed to be isotropic. Ratios of charge exchange to elastic cross sections for nitrogen were obtained from Phelps [10, 11]. The energy dependence of the symmetric charge exchange cross section is taken from Sakabe and Izawa [23] as

$$\sigma(\varepsilon) = \sigma_0(1 - 0.117 \log_{10} v) \tag{4}$$

where v is the ion velocity. The value for σ_0 is obtained from

$$\sigma_0 = \frac{q}{M v_t \mu N}$$

where M is the mass of the ion, v_t is the thermal speed of the ion, μ is the mobility of the ion, and N is the background gas density.

(b) Cross sections for exothermic reactions, or reactions where the threshold energy is equal to zero, vary inversely with velocity,

$$\sigma(\varepsilon) = \sigma_0(v_t/v) \tag{5}$$

in accordance with the Langevin–Gioumousis–Stevenson (LGS) model [19].

(c) Where transport data are not available, the elastic ion–molecule cross section is set to $10 \times 10^{-16}\,\mathrm{cm}^2$ at room temperature, with velocity dependence of $\sigma(v) = \sigma_0(v_t/v)$.

(d) Following Shultz and Armentrout [16], ion–molecule reactions which are endothermic are assumed to have an energy dependence of

$$\sigma(\varepsilon) = \sigma_0 \frac{(\varepsilon - \varepsilon_0)^n}{\varepsilon^m} \tag{6}$$

where ε_0 is the threshold energy for the process. In accordance with recommendations by Armentrout, we adopted $n = 0.5$ and $m = 1$. σ_0 is then determined either from the cited reaction rate coefficient, estimated from analogous reactions, or is considered a parameter. For the selected values of n and m, $\sigma_0 = 2\varepsilon_0^{0.5}\sigma_m$, where σ_m is the maximum cross section for the process and occurs at twice the threshold value.

In the absence of experimental data, the threshold energy for endothermic cross sections is typically taken as the difference between the ionization potentials for the two charge exchanging species. Although this threshold energy is often experimentally observed, there are also many instances where the threshold energy has a higher value. For example, the charge exchange reaction $Ar^+ + CF_4 \rightarrow CF_2^+ + 2F$ should thermodynamically have a threshold value of 4.77 eV, but is observed to have a threshold of 6.55 eV. The discrepency results from the fact that the charge exchange reaction proceeds through a transition state of CF_4^+ which predissociates to the observed fragments. The thermodynamic threshold energy is only observed if an appropriate transition state in the parent molecule exists at an energy corresponding to the sum of the thermodynamic threshold and ionization potential of the incident ion. Our use of the thermodynamic threshold in equation (6) is therefore a worst case analysis.

3. Ion energy distributions including endothermic processes

In this section we present results obtained from the hybrid model for pure argon, as well as for gas mixtures of He/N_2 (positive ions only), and $He/CF_4/H_2$ (negative and positive ions). Table 1 summarizes the conditions for all cases presented. The RF voltages are amplitudes

Table 1. Summary of cases.

System	Pressure (Torr)	RF voltage amplitude (V)	Electrode gap (cm)	Endothermic reactions?	Comment
Ar	0.5	65	3.0	no	
$He/N_2 = 99/1$					
	0.1	75	2.54	yes	
	0.5	75	2.54	yes	
	0.5	75	2.54	no	
	0.5	150	2.54	yes	
	0.5	50	2.54	yes	
	1.0	75	2.54	yes	
	0.5	75	2.54	yes	$V_{DC} = -50$ V
$He/CF_4/H_2 = 80/10/10$					
	0.2	100	2.54	yes	
	0.5	100	2.54	yes	
	1.0	100	2.54	yes	
	1.0	100	2.54	no	
	1.0	100	2.54	yes	no ion holes

of the applied sinusoidal potential and all cases have a frequency of 13.56 MHz. With one exception, all have an electrode separation of 2.54 cm. These values correspond to the operating conditions of the Gaseous Electronics Conference Reference Cell. Unless otherwise stated, the discharge is symmetric. Table 2 lists the ion and neutral reactions used in the simulation with their corresponding rate coefficients or cross sections. Electron interactions are not included since they have been previously tabulated [20]. For charge exchange reactions, the cross section, σ_0 or σ_m, is given instead of the rate coefficient, depending on whether the reaction is exothermic or endothermic respectively.

The benchmark case for validating our model is an argon discharge. Our calculated IED for Ar^+ is shown in figure 1 and agrees well with the experimental results of Lui *et al* [4]. The fall-off of the high-energy tail for the Ar^+ IED is slightly more rapid for our calculations.

IEDs for He/N_2 plasmas were calculated for varying pressures (100 mTorr to 1 Torr) and voltages (50 to 150 V) as being representative of a multicomponent electropositive RF discharge. The endothermic reactions of interest are N^+ and N_2^+ charge exchanging with He. Our base case is a mixture of $He/N_2 = 99/1$, RF voltage of 75 V, and a pressure of 500 mTorr. These conditions were selected so that N_2^+ collisions in the bulk plasma are largely elastic, due to the small mole fraction of N_2, while the predominance of collisions of He^+ in the bulk are symmetric charge exchange. Previous studies [12–19] have shown that inelastic charge exchange cross sections for a variety of gases (e.g. Ar^+ in SiF_4) have peak values of tens of $Å^2$. The intent of this work is to demonstrate the potential effects of large inelastic charge exchange cross sections in simpler systems for which sufficient electron impact cross sections are known so that a full discharge simulation can be performed. We therefore have chosen generously large endothermic cross sections for N_2^+ and N^+ on He for demonstration purposes, as shown in table 2.

Various time averaged plasma parameters as a function of position between the electrodes are shown in figure 2 for the base case. The electron temperature, shown in figure 2(*a*), is nearly uniform at ≈ 2 eV, with

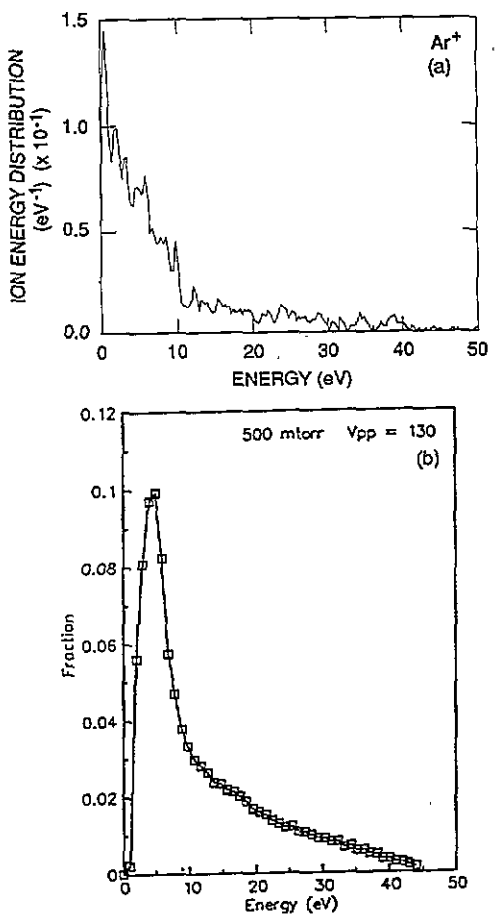

Figure 1. Comparison between (*a*) MCFH simulation and (*b*) experimental results for a 0.5 Torr pure argon RF discharge with 65 V applied RF potential (amplitude). The IED for the simulation has been normalized relative to the total number of ions in the discharge. The experimental results are from [4].

Table 2. Heavy particle reactions included in the model.

Process	Rate coefficient[a]	σ[b]	Threshold energy ε_0 (eV)	Reference
Ar				
$Ar^* + Ar^* \rightarrow Ar^* + Ar + e$	5×10^{-10}		0	24
$Ar^+ + e + e \rightarrow Ar^* + Ar$	$5 \times 10^{-27} T_e^{-4.5}$ cm^6 s^{-1}		0	c
$Ar^+ + Ar \rightarrow Ar_2^+$	4×10^{-15}		0	25
$Ar^+ + Ar \rightarrow Ar + Ar^+$		5.2×10^{-15}	0	d
He/N_2				
$He^* + He^* \rightarrow He + He^+ + e$	1.5×10^{-9}		0	26
$He^* + He \rightarrow He + He$	5.8×10^{-15}		0	27
$He^+ + He \rightarrow He + He^+$		4.4×10^{-15}	0	e
$N_2^* + N_2^* \rightarrow N_2^* + N_2$	1.36×10^{-9}		0	28
$N_2(v) + N_2(v) \rightarrow N_2 + N_2(v)$	1×10^{-12}		0	29
$N_2(v) + N_2 \rightarrow N_2 + N_2$	3×10^{-22}		0	29
$N_2^* + N_2 \rightarrow N_2 + N_2$	1.9×10^{-13}		0	30
$N_2^+ + N_2 \rightarrow N_2 + N_2^+$		6.0×10^{-15}	0	f
$N_2^+ + N \rightarrow N^+ + N_2$	1×10^{-11}		0	31
$N_2^+ + N_2 + He \rightarrow N_4^+ + He$	1.9×10^{-29} cm^6 s^{-1}		0	31
$He^+ + N_2 \rightarrow He + N_2^+$	5×10^{-10}		0	31
$He^+ + N_2 \rightarrow He + N^+ + N$	7×10^{-10}		0	31
$He^+ + N_2(v) \rightarrow He + N_2^+$	5×10^{-10}		0	31
$He^+ + N_2(v) \rightarrow He + N^+ + N$	7×10^{-10}		0	31
$He^* + N_2 \rightarrow N_2^+ + He + e$	7×10^{-11}		0	32
$He^* + N_2(v) \rightarrow N_2^+ + He + e$	7×10^{-11}		0	32[g]
$N_2^+ + He \rightarrow He^+ + N_2$		3×10^{-15}	9.01	h
$N^+ + He \rightarrow He^+ + N$		3×10^{-15}	10.06	h
$He/CF_4/H_2$				
$He^* + He^* \rightarrow He^+ + He + e$	1.5×10^{-9}		0	26
$He^* + He \rightarrow He + He$	5.8×10^{-15}		0	27
$He^+ + He \rightarrow He + He^+$		4.4×10^{-15}	0	e
$F^- + CF_3 \rightarrow CF_3 + F$	5×10^{-8}		0	h
$F^- + H_2^+ \rightarrow H_2 + F$	5×10^{-8}		0	h
$F^- + H^+ \rightarrow H + F$	5×10^{-8}		0	h
$F^- + H_3^+ \rightarrow H_2 + F$	5×10^{-8}		0	h
$F^- + He^+ \rightarrow He + F$	5×10^{-8}		0	h
$H_2^+ + H_2 \rightarrow H_3^+ + H$	1.5×10^{-9}		0	33
$H_2^+ + H_2 \rightarrow H_2 + H_2^+$		1.5×10^{-15}	0	e
$He^* + H_2 \rightarrow H_2^+ + He + e$	3.7×10^{-11}		0	32
$He^* + CF_4 \rightarrow CF_3^+ + He + F + e$	5×10^{-12}		0	h
$He^+ + H_2 \rightarrow H_2^+ + He$	1×10^{-13}		0	31
$He^+ + CF_4 \rightarrow He + CF_3^+ + F$	1×10^{-9}		0	h
$CF_3^+ + CF_4 \rightarrow CF_3 + CF_3^+ + F$		1×10^{-16}	7.35	19
$H^+ + H_2 \rightarrow H_2^+ + H$		1.5×10^{-16}	2.7	34
$CF_3^+ + He \rightarrow He^+ + CF_3$		3×10^{-16}	15.7	12[i]
$H^+ + He \rightarrow He^+ + H$		1.7×10^{-16}	11.2	34
$H_2^+ + He \rightarrow H_2^+ + He^+ + e$		1.2×10^{-16}	24.6	34

*Listed value is a two-body effective collision rate; actual rate coefficient for $Ar^+ + Ar + M \rightarrow Ar_2^+ + M$ is 2.5×10^{-31} cm^6 s^{-1}.

[a]Rate coefficients have units of cm^3 s^{-1} unless otherwise noted.

[b]For symmetric charge exchange reactions, $\sigma = q/Mv\mu N$ with energy dependence given by equation (4). For exothermic charge exchange reactions, $\sigma = \sigma_0$ with energy dependence given by equation (5). For endothermic reactions, $\sigma = \sigma_m$ with energy dependence given by equation (6).

[c]T_e is the electron temperature in eV.

[d]Charge exchange to momentum transfer ratio determined by Phelps [10].

[e]Charge exchange to momentum transfer ratio assumed to be 90/10.

[f]Charge exchange to momentum transfer ratio determined by Phelps [11].

[g]N_2 analogy for reference [32].

[h]Estimate.

[i]He analogy for reference [12].

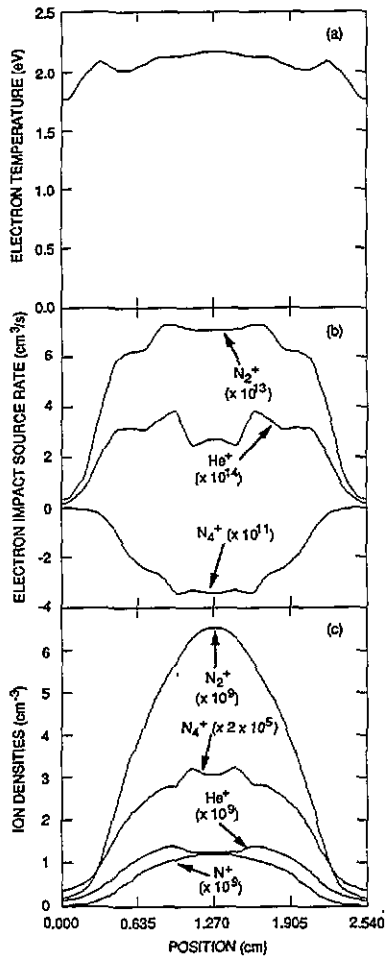

Figure 2. Plasma parameters for $He/N_2 = 99/1$ discharge at 0.5 Torr and 75 V applied RF voltage amplitude. The discharge parameters are modelled after the GEO Reference Cell, with gap spacing of 2.54 cm and a frequency of 13.56 MHz. All results are averaged over the centre line. The values in parentheses are the multiplying values for the vertical scale. (*a*) Electron temperature. (*b*) Ionization rates based on electron impact collsions. (*c*) Ion densities.

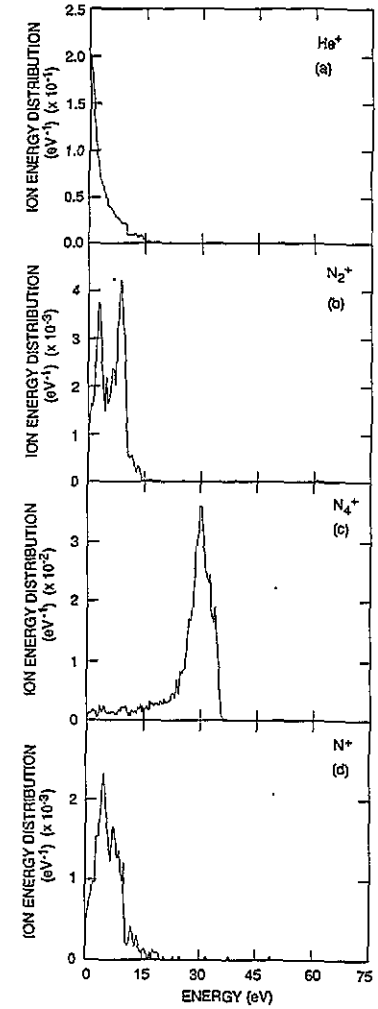

Figure 3. Computed IEDs for the discharge conditions in figure 2. (*a*) He^+, (*b*) N_2^+, (*c*) N_4^+, and (*d*) N^+. The IEDs are normalized with respect to the total number of ions in the plasma. N_2^+ and N^+ undergo endothermic collisions and have cut-off IEDs.

slight heating at the plasma–sheath boundaries and in the centre of the bulk of the plasma. Source functions for electron impact processes are shown in figure 2(*b*). N_2^+ and He^+ have large positive rates resulting from electron impact dissociation of ground state and metastable electronic states in both cases. N_2^+ and He^+ have their maximum sources displaced towards the sheath edges, but are otherwise fairly uniform, largely a result of the dominance of multistep ionization. The small spatial structure of these source functions results from noise in the EMCS. N_4^+ is not directly formed by electron impact but rather results from ion–molecule reactions. Its negative source results from dissociative recombination. Ion densities are shown in figure 2(*c*). N_2^+ has the highest density in the bulk plasma ($6.5 \times 10^9\,cm^{-3}$), in spite of its lower rate of production by electron impact, due to Penning and charge exchange collisions from He* and He^+ with N_2 which generate N_2^+. Charge exchange of N_2^+ with N_2 is largely responsible for the moderately large density of N^+, since its source function by electron impact is small. N_4^+ is formed by three-body collisions of N_2^+, N_2 and a stabilizing collision partner. As a result, its density is small ($6.5 \times 10^5\,cm^{-3}$) at these low pressures. Nevertheless, N_4^+ is a good tracer species for the IED of a heavy ion which undergoes largely elastic collisions. The spatial distribution of He^+ closely resembles that of its source function, a consequence of a moderately rapid rate of charge exchange with N_2.

IEDs for the base He/N_2 case are shown in figure 3. The IED for helium ions is dominated by charge exchange collisions with He and thus exhibits a low-energy peak followed by a sharp drop off in the high-energy tail. The IED for N_2^+ shows two peaks at low energies. The IED is 'cut off' at ≈ 9 eV, which corresponds to the threshold energy for endothermic charge exchange with helium. This 'cut-off' in the IED is similar to, but not completely analogous to, 'cut-off' electron energy distributions (EEDs) which occur at the inelastic thresholds for electron impact excitation. The electron undergoing the inelastic collision which results in a 'cut-off' EED loses the threshold energy and 'falls' to a lower energy which populate the bulk of the EED. The ion which undergoes

an inelastic charge exchange collision is similarly removed from the upper portion of the IED. The ion does not, however, populate the lower portion of the original IED since its identity is changed as a result of the collision. The ion does, however, populate the low-energy portion of the IED of the product ion. In our base case, the low-energy portion of IED for He^+ is significantly increased due to the generation of thermal He^+ ions by endothermic charge exchange of N_2^+ with He which occurs deep in the sheath.

The IED for N^+ is cut off near 10 eV in a similar fashion to that observed for N_2^+. This cut-off is again due to the endothermic charge exchange reaction with helium. On the other hand, N_4^+ ions, which we have selected not to undergo endothermic collisions, have a markedly different distribution. The IED is characteristic of heavy ions traversing an RF sheath undergoing only elastic collisions. The maximum energy is approximately half the RF voltage amplitude which corresponds to the average sheath potential. N_4^+ is actually fairly collisional with its primary collision partner being He. The rate of momentum transfer during these elastic collisions is low due to the large mass difference between N_4^+ and He. Hence there is little degradation of the N_4^+ energy.

The details of the IEDs critically depend on both the shape and magnitude of the endothermic cross sections. For our base case we have selected large cross sections for endothermic processes for demonstration purposes. For comparison, IEDs for nitrogen ions are shown in figure 4 when excluding endothermic processes. IEDs are also shown in figure 5 when varying the maximum cross section for N_2^+ charge exchange with He from zero to $3 \times 10^{-15}\,cm^2$. In the absence of endothermic processes, the IEDs for N_2^+, N^+ (figures 4(*a*) and (*b*)), and N_4^+ (figure 3(*c*)) have approximately the same shape. This results from the fact that the majority of collisions in the sheath are elastic collisions with He, for which the rate of momentum transfer is small due to the large mismatch in masses. N_4^+ undergoes only elastic collisions and is the heaviest of the ions, which results in the lowest rate of momentum transfer. The IED for N_2^+ is degraded relative to N_4^+ due to charge exchange collisions with N_2. The IED for N^+ is somewhat degraded with respect to N_4^+ as a result of a more rapid rate of elastic momentum transfer to He resulting from the closer match in masses. The IED for N^+ also has a bimodal shape resulting from N_2^+ charge exchange collisions in the sheath, which produce N^+ and which then strike the substrate with less than the full sheath potential. In the absence of endothermic processes, the flux of N_2^+ and N^+ is larger, and the flux of He^+ smaller. This is caused by the fact that endothermic charge exchange in the sheath depletes the nitrogen ions while providing a source for He^+.

IEDs for N_2^+ are shown in figure 5 for different values of the peak cross section for endothermic charge exchange with He. The thickness of the sheath for these conditions is $\simeq 0.3$ cm. For a helium pressure of 0.5 Torr, the sheath is therefore collisional for a given process when its cross section for reaction with He exceeds

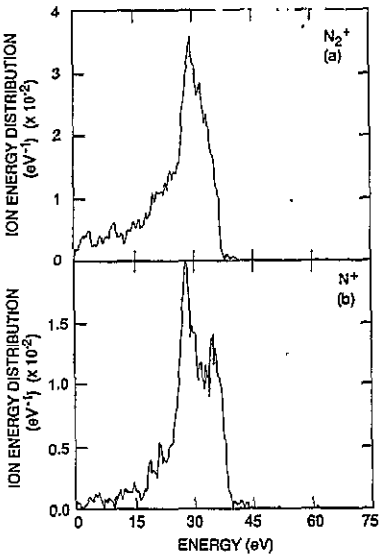

Figure 4. IEDs for the same conditions as in figure 2, except that all endothermic processes have been excluded. (*a*) N_2^+, (*b*) N^+, and N_4^+ (figure 3(*c*)) all exhibit nearly the same shape with a peak in the IED near 30 eV.

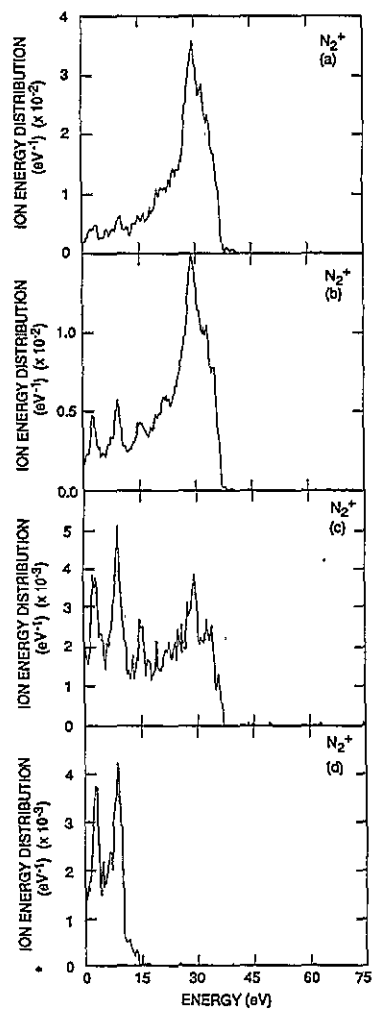

Figure 5. Comparison of IEDs for N_2^+ in a He/N_2 discharge for the conditions of figure 2 while varying the values of the endothermic cross sections. See table 2 for the pertinent reactions. (*a*) $\sigma_m = 0$ (exothermic processes only), (*b*) $\sigma_m = 9 \times 10^{-17}\,cm^2$, (*c*) $\sigma_m = 3 \times 10^{-16}\,cm^2$, and (*d*) $\sigma_m = 3 \times 10^{-15}\,cm^2$. The sheath becomes collisional with respect to endothermic charge exchange for $\sigma_m \gtrsim 10^{-15}\,cm^2$.

$2 \times 10^{-16}\,cm^2$. This scaling is confirmed by the results in figure 5. The IEDs are similar for $\sigma_m < 1 \times 10^{-16}\,cm^2$ (figures 5(*a*) and (*b*)), and are largely collisionless for endothermic collisions with He. For $\sigma_m > 1 \times 10^{-16}\,cm^2$, the portion of the IED above the inelastic threshold degrades relative to the lower portion of the IED. For $\sigma_m > 10 \times 10^{-16}\,cm^2$, the IED is severely cut-off. The flux of N_2^+ to the substrate decreases by $\simeq 100$ over the range of cross sections considered in figure 5. Commensurately, the flux of He^+ increases as σ_m increases since the collisions which deplete N_2^+ replenish He^+.

The IEDs for N_2^+ shown in figures 5(*b*)–(*d*) appear to increase at low energy. This increase in the normalized IED is not a result of a net increase of N_2^+ ions at low energy, but is due to the depletion of the IED which is above the inelastic threshold. Note that structure in the IED at energies less than the inelastic threshold is retained and magnified as the endothermic cross section increases, a consequence of the depletion of the high-energy N_2^+ ions. The IEDs for N^+ (see figure 6) undergo similar transformations with increasing σ_m and are again cut off for $\sigma_m > 10 \times 10^{-16}\,cm^2$.

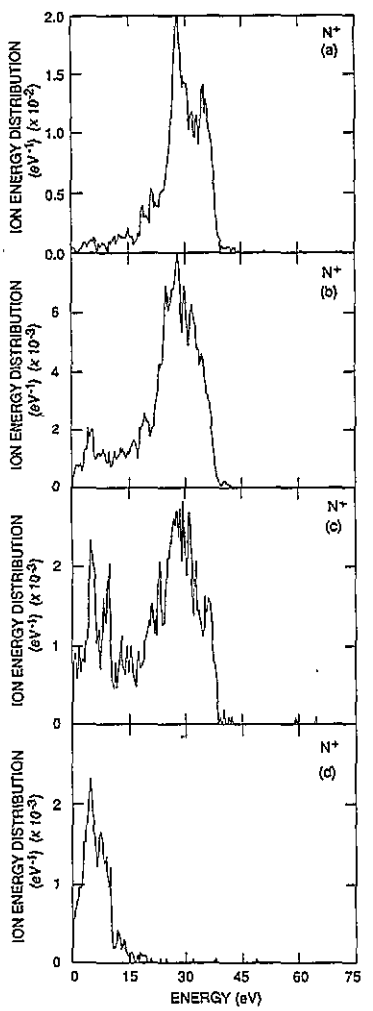

Figure 6. IEDs for N^+ in He/N_2 discharges while varying the peak value of the endothermic charge exchange cross section. (*a*) $\sigma_m = 0$ (no endothermic processes), (*b*) $\sigma_m = 9 \times 10^{-17}\,cm^2$, (*c*) $\sigma_m = 3 \times 10^{-16}\,cm^2$, and (*d*) $\sigma_m = 3 \times 10^{-15}\,cm^2$. Note the apparent growth in the lower energy portion of the IED due to the decay of the high energy portion.

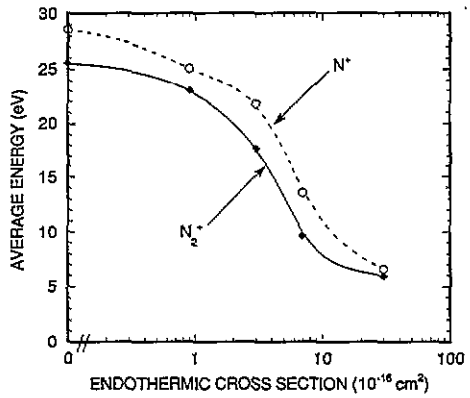

Figure 7. Average energies of N^+ and N_2^+ striking the electrodes for the IEDs shown in figures 5 and 6.

The average energy of N_2^+ and N^+ ions as they strike the substrate are shown in figure 7 as a function of the maximum cross section σ_m of their respective endothermic processes. When excluding endothermic processes, the average energy is slightly less than half of the RF amplitude for the lighter ion. Increasing σ_m results in the distribution function taking on a cut-off behaviour, reducing the average energy to approximately half of the threshold energy.

IEDs for N_2^+ for the discharges sustained in He/N_2 are shown in figure 8 for pressures ranging from 0.1 to

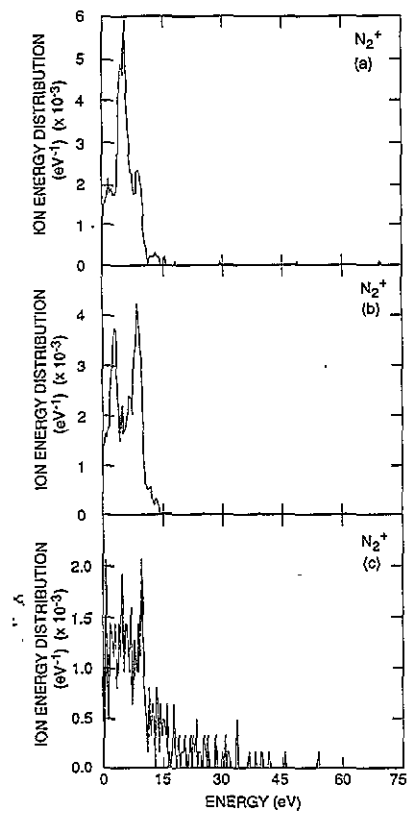

Figure 8. IEDs for N_2^+ for various pressures in He/N_2 discharges. (*a*) 1 Torr, (*b*) 0.5 Torr, and (*c*) 0.1 Torr. All cases have an applied RF amplitude of 75 V. The N_2^+ becomes depleted as the pressure is decreased to 100 mTorr due to endothermic charge exchange. This trend will reverse at sufficiently low pressures such that the sheath is collisionless.

1 Torr. When considering endothermic processes, the IED is 'cut off' at the threshold energy for charge exchange with He at $\simeq 9$ eV. This cut-off character is retained at pressures as low as 0.1 Torr for the demonstration system. In the absence of endothermic processes, the energy of N_2^+ ions striking the substrate should increase with decreasing pressure since the sheath becomes less collisional. With endothermic processes, N_2^+ ions which are accelerated to higher energies at lower pressures are *more likely* to suffer endothermic charge transfer collisions with He, and therefore may become more collisional. When these collisions occur, ions are removed from the N_2^+ flux. Therefore one actually sees a decrease in the flux of N_2^+ with decreasing pressure, at least to values as low as 100 mTorr. The IED shown in figure 8(*c*) for 0.1 Torr shows a higher number of ions with energy greater than the cut-off, a consequence of N_2^+ ions which manage to collisionlessly traverse the sheath. However, the number of N_2^+ ions is in general greatly depleted. (The noise in the IED shown in figure 8(*c*) results from the small number of N_2^+ pseudoparticles which survive to reach the substrate.) Lowering the pressure from 1 Torr to 0.1 Torr decreases the N_2^+ flux by more than an order of magnitude. This trend will reverse at sufficiently low pressures (tens of millitorr) where the sheath becomes collisionless even for large σ_m, and the N_2^+ flux will become more energetic.

For systems in which elastic or symmetric charge exchange collisions dominate, the average energy of ions striking the substrate increases with increasing RF amplitude since these cross sections typically decrease with increasing energy. Therefore, higher energy ions suffer fewer collisions. This scaling is shown in figure 9 where the IED for N_4^+ (chosen for demonstration purposes to have only elastic collisions) is plotted for RF amplitudes of 50–150 V. The peak of the distribution increases with increasing RF amplitude, as does the average ion energy, shown in figure 10.

However, for ion energies of less than tens to hundreds of eV, endothermic cross sections generally increase with increasing energy above threshold. Therefore, the IED either retains its cut-off character or becomes cut off with increasing RF amplitude since a larger fraction of the ions sample the endothermic cross sections. For example, the average energy of N_2^+ striking the substrate (shown in figure 10) is a weak function of RF amplitude. This effect is more severe for endothermic ion collisions than for the analogous cut-off processes for EEDs. This result from the fact that ions which undergo an endothermic collision are removed from the IED, whereas an electron suffering an inelastic collision merely loses energy and falls to a lower energy of the distribution. Again, we expect these scalings to reverse at sufficiently low pressure (tens of millitorr) where the sheath is collisionless.

The hybrid model has the capability of addressing asymmetric RF discharges by specifying a DC bias on the powered electrode and separately collecting statistics in the IMCs for pseudoparticles that strike the grounded or powered electrodes. We investigated IEDs in asymmetric

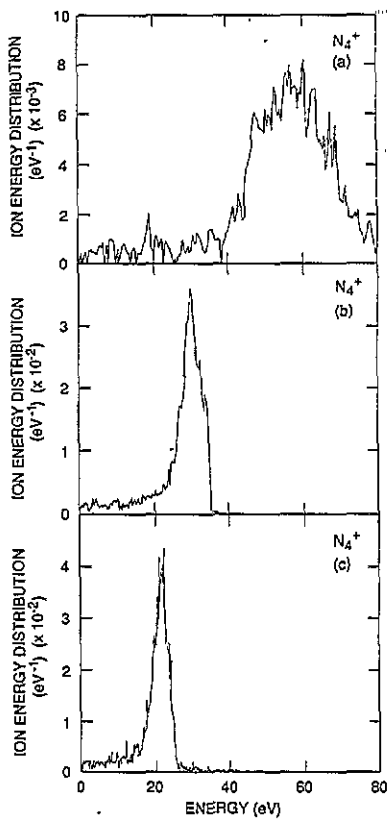

Figure 9. IEDs for N_4^+ in 0.5 Torr He/N_2 discharges with varying applied RF potential (*a*) 150 V, (*b*) 75 V, (*c*) 50 V.

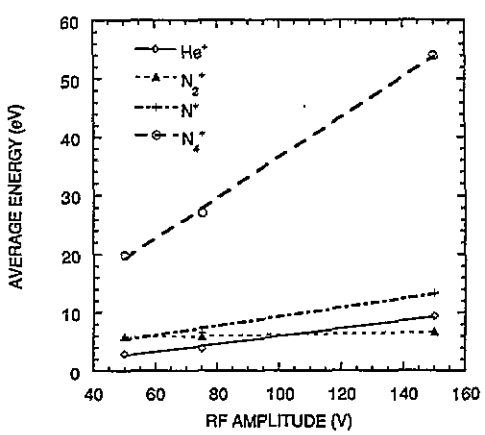

Figure 10. Average energies of ions striking the electrodes in 0.5 Torr He/N_2 discharges for various applied RF voltages. Energies are computed from the IEDs shown in figure 9.

discharges as a demonstration of the potential for endothermic processes to alter the ion flux incident on opposing electrodes in a single discharge significantly. Our sample case for an asymmetric discharge uses the same conditions as for figure 2 with the addition of a bias of -50 V on the powered electrode.

The time-averaged charged particle densities and electric fields are shown in figure 11 for the asymmetric discharge. (The grounded electrode is at $x = 0$ cm and the powered electrode is at $x = 2.54$ cm.) The sheath thickness on the powered electrode is roughly double that of the grounded electrode, resulting in corresponding decreases in charged particle densities adjacent to

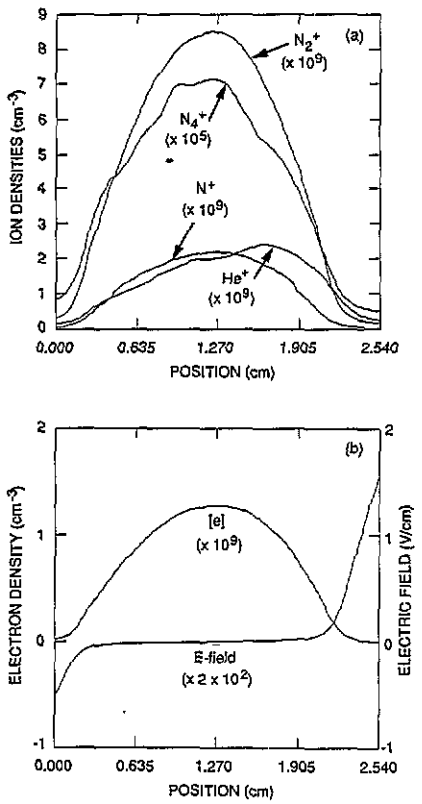

Figure 11. Time-averaged densities and electric field in a $He/N_2 = 99/1$ discharge at 0.5 Torr, $V_{RF} = 75$ V as a function of position. The grounded electrode is at $x = 0$ cm. The electrode at $x = 2.54$ cm has a DC bias of -50 V. Numbers in parentheses are the multiplying factors for the vertical scale. (*a*) Ion densities. (*b*) Electron density and electric field. The larger sheath at the powered electrode causes some asymmetry in the densities of short lived species.

the powered electrode. The spatial distribution of He^+ is the most asymmetric of the charged particles. In general, species having higher inelastic threshold energies are more sensitive to the DC bias. This results from the higher rate of stochastic heating of electrons which occurs near the powered electrode whose sheath oscillates with a larger amplitude. The fact that He^+ quickly charge exchanges with N_2 exacerbates the consequences of asymmetric excitation. These ions nearly react 'in place' and therefore do not homogenize their spatial distribution by diffusion. Ions having a lower ionization potential, such as N_2^+, are not as sensitive to the DC bias. But, more importantly, their longer mean free paths for identity changing charge exchange reactions (as opposed to symmetric charge exchange) allows for diffusion to homogenize any asymmetries in their generation.

Calculated IEDs for ions striking the grounded and powered electrodes are shown in figure 12 for He^+ and N_4^+, and figure 13 for N_2^+ and N^+. He^+ (which undergoes symmetric charge exchange) is less sensitive to the DC bias on the powered electrode since its mean free path is short in any event. The IED for N_4^+ (which in this reaction scheme suffers only elastic collisions) shifts to higher energy by nearly the full DC bias.

Since in our reaction scheme N_2^+ and N^+ undergo endothermic charge exchange reactions with He, these ions display different behaviour impacting on the powered electrode compared to He^+ and N_4^+. The DC bias at the powered electrode accelerates ions to energies significantly above the inelastic thresholds. For the energies of interest, the endothermic cross sections increase with increasing energy. As a result, the probability for identity changing charge exchange reactions increases, and the net flux of N_2^+ and N^+ reaching the powered electrode decreases. The numerical noise in IED for N^+

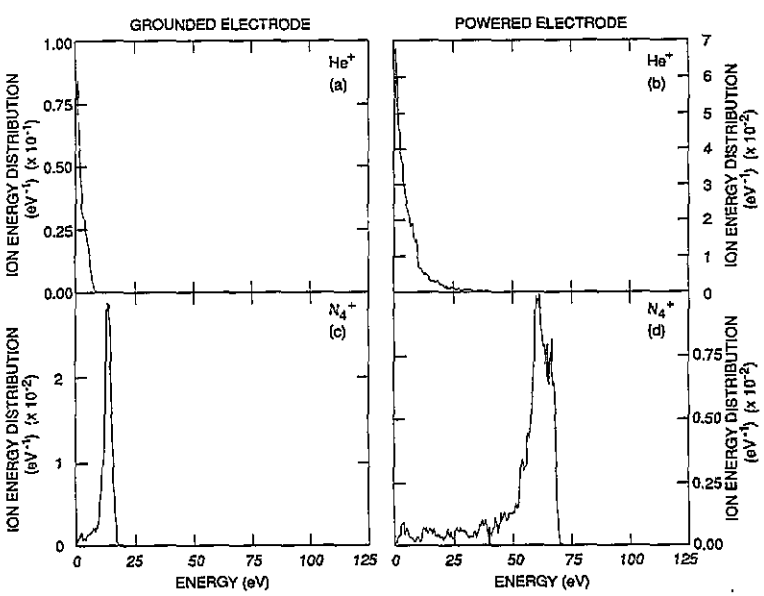

Figure 12. IEDs in a $He/N_2 = 99/1$ discharge at 0.5 Torr, $V_{RF} = 75$ V, and $V_{DC} = -50$ V. IEDs in the left column are for ions striking the grounded electrode. IEDs in the right column are for ions striking the powered electrode. (*a*) and (*b*) are IEDs for He^+; (*c*) and (*d*) are IEDs for N_4^+.

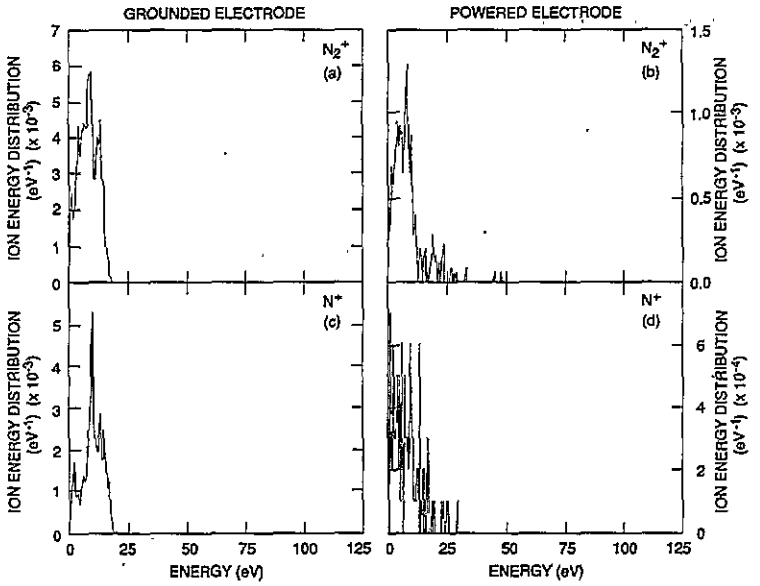

Figure 13. IEDs for N_2^+ and N^+ for the same conditions as in figure 12. The left column is for the grounded electrode. The right column is for the powered electrode

impacting on the powered electrode reflects the large rate of depletion of N^+ resulting from the endothermic process.

IEDs were also examined in $He/CF_4/H_2$, mixtures which contain both positive and negative ions. Our standard conditions are $He/CF_4/H_2 = 80/10/10$, 500 mTorr, and an RF amplitude of 100 V. Although the negative ion density we calculated is 10–50 times the electron density, a negligible number of the negative ions actually strike the substrate since they are trapped by the positive plasma potential. In our simulations, we collected only a few negative ion pseudoparticles. These negative ions were generated by electron impact within a mean free path of the electrode with a statistically large velocity (randomly chosen from a Maxwellian having the gas temperature) which was directed towards the electrode. The collected ions typically had a few tenths of an eV of energy.

IEDs for the standard conditions are shown in figure 14. IEDs for CF_3^+ for total gas pressures of 0.2–1.0 Torr are shown in figure 15. The IED for He^+ peaks at low energies due to a large rate of symmetric charge exchange. The IED also peaks due to the sources of He^+ from endothermic processes in the sheath. The large low-energy component in the IED of H_3^+ (assumed to undergo only elastic collisions) reflects there being a high number of large angle scattering events and large rate of momentum transfer which it suffers in elastic collisions with He. H_2^+ ions are depleted by charge exchanging with H_2, creating H_3^+ ions. As a result, H_2^+ ions do not reach the electrodes in appreciable quantities. The H^+ ions are formed predominantly by electron impact on H_3^+ ions. Since this is a third-order process, few H^+ ions are formed and again their flux to the electrodes is small.

CF_3^+ ions are the most abundant and heaviest of the ions. Elastic collisions with He result in little momentum transfer. A large inelastic threshold for charge exchange in He results in a CF_3^+ having an IED at 0.2 Torr which appears collisionless with its peak value at nearly half the RF amplitude. At 0.5 Torr, inelastic collisions with He and CF_4 begin to degrade the maximum in the IED.

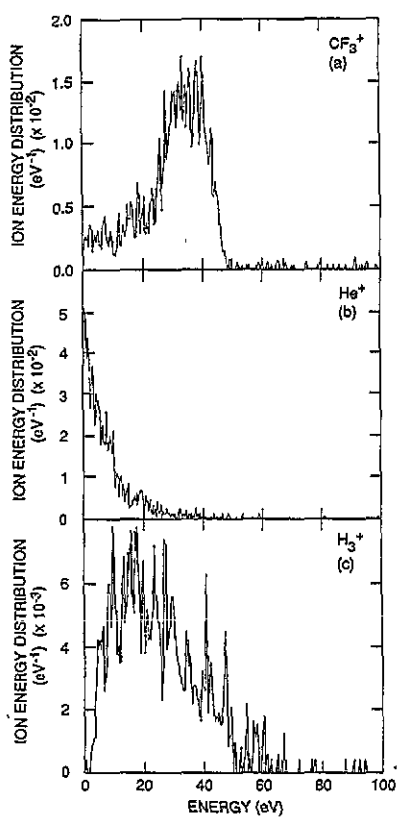

Figure 14. IEDs for an $He/CF_4/H_2 = 80/10/10$ RF discharge at 0.5 Torr with an applied RF amplitude of 100 V. (*a*) CF_3^+, (*b*) He^+, and (*c*) H_3^+. H_2^+ and H^+ do not arrive at the electrodes in appreciable quantities due to charge exchange collisions.

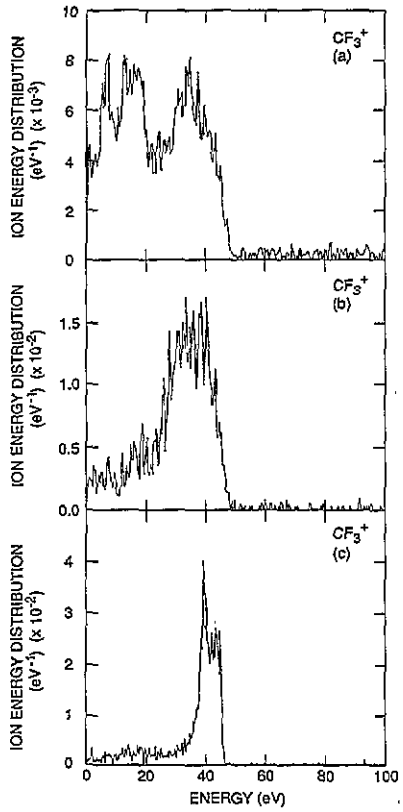

Figure 15. IEDs for CF_3^+ while varying pressure in an $He/CF_4/H_2$ discharge. All other parameters are the same as in figure 14. (*a*) 1 Torr, (*b*) 0.5 Torr, and (*c*) 0.2 Torr.

At 1.0 Torr, the high-energy component of the IED of CF_3^+ has been severely depleted relative to the low-energy portion of the IED.

The contributions of ion holes to the IED of CF_3^+ are shown in figure 16 where results for discharges at 1 Torr when excluding endothermic processes or excluding ion holes are plotted. When excluding endothermic processes, the high-energy component of the IED is maintained even at 1 Torr. The flux of CF_3^+ ions reaching the substrate increases by about an order of magnitude when excluding endothermic processes, with a commensurate decrease in the flux of He^+ ions. One might expect that the IED in figure 16(*a*) (no endothermic processes, high pressure) should be nearly identical to figure 15(*c*) (with endothermic processes, low pressure) because both represent conditions which are inelastically collisionless. Instead, the high-pressure (no endothermic processes) IED is degraded in energy. This results from the large rate of momentum transfer collisions of CF_3^+ with CF_4 which occur at the higher pressure.

The change in the IED for CF_3^+ with and without endothermic processes is quantified in the 'difference-IED' shown in figure 16(*b*). The difference-IED is obtained by renormalizing the IEDs with and without endothermic processes to unity, and subtracting the IED without endothermic processes from the IED with endothermic processes. The difference-IED shows that CF_3^+ retains its high-energy component in the absence of endothermic processes. There are, however, a few ions which traverse the sheath without having collisions, so that the difference-IED at very high energies show little variation between the IEDs.

When excluding ion holes from the simulation, we fail to remove trajectories in phase space resulting from ion–fluid collisions. For these conditions the majority of the ion holes are generated by ion–ion neutralization rather than by electron impact processes such as dissociative recombination. Since ion holes account for fewer

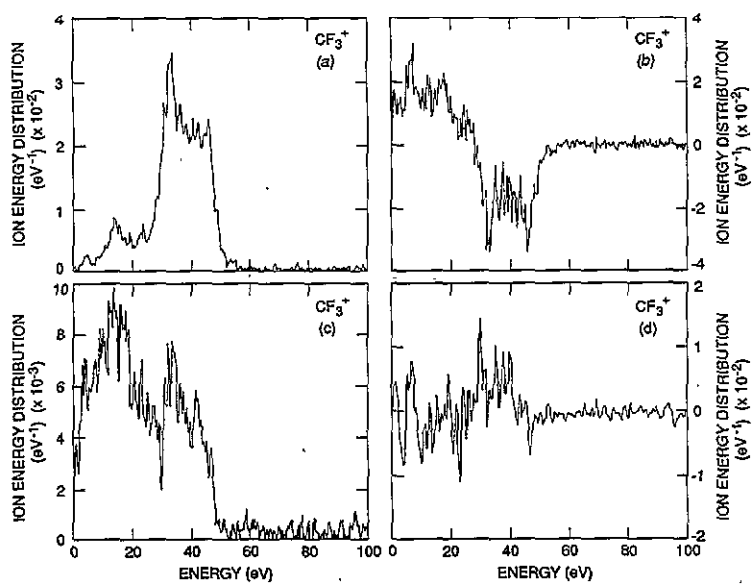

Figure 16. IEDs for CF_3^+ using different modelling strategies in an $He/CF_4/H_2$ discharge at 1 Torr. (*a*) Ion holes are used in the HMCF routine but endothermic processes are excluded. (*b*) Difference-IED obtained by subtracting the IED without endothermic processes from the IED with endothermic processes (figure 15(*a*)). (*c*) Endothermic processes are included, but ion holes are not used in HMCF, (*d*) Difference-IED obtained by subtracting the IED without ion holes from the IED with ion holes.

than 10% of the total number of pseudoparticles, the total flux of CF_3^+ striking the substrate does not appreciably change. Comparing the IEDs in figure 15(*a*) and figure 16(*c*), we find that the IED without ion holes has a larger flux of low-energy ions (<20 eV). The difference-IED (IED without ion holes subtracted from the IED with ion holes) is also shown in figure 16(*d*). The lower energy portion is generally more negative, meaning that the case without ion holes has a larger number of low-energy ions striking the substrate than the case with ion holes. This means that the trajectories we have removed from phase space by including ion holes are predominantly those which produce lower energy ions. This may result from the fact that the majority of collisions which deplete ions (by ion–ion or electron–ion collisions) occur near the maximum in the plasma density, and are many free paths from the substrate. Therefore removing trajectories from these locations is more likely to reduce the flux of ions which, on average, are more collisional.

4. Concluding remarks

We have presented a hybrid Monte Carlo–fluid model of an RF discharge which includes electron- and ion-pseudoparticles for analysis of multicomponent gas mixtures. Ion hole pseudoparticles have been introduced as a method to account for trajectories in phase space which should be removed during pseudoparticle–fluid collisions. We found, for example, that when ion holes were not included, ion energy distributions were artificially heated. Implementing ion holes is computationally inexpensive and these particles were approximately 10% of the total number of pseudoparticles in the quasisteady state. We also included endothermic charge exchange reactions to account for ion changing reactions which may occur in collisional sheaths.

The model was applied to analyse the Gaseous Electronics Conference Reference Cell, having an electrode spacing of 2.54 cm and RF applied voltage at 13.56 MHz. Ions undergoing endothermic processes in He/N_2 discharges had cut-off energy distributions, somewhat analogous to cut-off electron energy distributions. Lowering the pressure from higher values to 100 mTorr led to more energetic ions in the sheath, which consequently led to more endothermic charge exchanges. Hence the flux of ions undergoing endothermic reactions to the electrodes was smaller at lower pressures. This trend will reverse at sufficiently low pressures (tens of millitorr) at which the sheath is not collisional.

Larger values of the endothermic cross sections depleted the high-energy portion of the IED and caused the lower energy structures of the IEDs to predominate. Peak cross sections greater than $\approx 7 \times 10^{-16}$ cm^2 for reaction with He were sufficient to deplete the IEDs of high-energy nitrogen ions at 500 mTorr.

As a result of the endothermic processes, the IEDs striking the opposing electrodes in asymmetric discharges may have significantly different characteristics. Ions which do not undergo endothermic charge exchange processes have IEDs with higher average energies at the powered electrode which has a DC bias. In contrast, ions which undergo endothermic processes can be significantly depleted at the powered electrode due to their being accelerated above the inelastic threshold.

Acknowledgments

We thank Debbie Thomas for her technical support in this study, J Olthoff and S Radovanov for providing appreciated insights about IEDs in RF discharges. We also thank Herb Sawin for permission to use his results as a comparison for our argon discharge calculations. Debbie Thomas was supported by the NSF Research Experience for Undergraduates Program. The work of Hwang and Kushner was supported by the University of Wisconsin Engineering Research Center for Plasma Aided Manufacturing, the National Science Foundation (ECS91-09326, CTS91-13215), the Semiconductor Research Corporation, and IBM East Fishkill Facility.

References

[1] Manenschijn A and Goedheer W J 1991 *J. Appl. Phys.* **69** 2923
[2] Kushner M J 1985 *J. Appl. Phys.* **58** 4024
[3] Thompson B E, Sawin H H and Fisher D A 1988 *J. Appl. Phys.* **63** 2241
[4] Liu J, Huppert G L and Sawin H H 1990 *J. Appl. Phys.* **68** 3916
[5] Ingram S G and St J Braithwaite N 1988 *J. Phys. D: Appl. Phys.* **21** 1496
[6] Kuypers A D and Hopman H J 1990 *J. Appl. Phys.* **67** 1235
[7] Manenschijn A, Janssen G C A M, van der Drift E and Radelaar S 1991 *J. Appl. Phys.* **69** 1253
[8] Field D, Klemperer D F, May P W and Song Y P 1991 *J. Appl. Phys.* **70** 72
[9] Toyoda H, Kojima H and Sugai H 1989 *Appl. Phys. Lett.* **54** 1507
[10] Phelps A V 1992 *J. Phys. Chem. Ref. Data* **21** 883
[11] Phelps A V 1991 *J. Phys. Chem. Ref. Data* **20** 557
[12] Fisher E R and Armentrout P B 1991 *J. Phys. Chem.* **95** 6118
[13] Boo B H and Armentrout P B 1991 *J. Phys. Chem.* **91** 5777
[14] Fisher E R and Armentrout P B 1991 *Chem. Phys. Lett.* **179** 435
[15] Fisher E R and Armentrout P B 1991 *J. Phys. Chem.* **95** 4795
[16] Shultz R H and Armentrout P B 1991 *Chem. Phys. Lett.* **179** 429
[17] Shultz R H and Armentrout P B 1992 *J. Chem. Phys.* **96** 1036
[18] Shultz R H and Armentrout P B 1992 *J. Chem. Phys.* **96** 1046
[19] Fisher E R, Weber M E and Armentrout P B 1990 *J. Chem. Phys.* **92** 2296
[20] Sommerer T J and Kushner M J 1992 *J. Appl. Phys.* **71** 1654

[21] Sommerer T J and Kushner M J 1992 *J. Vac. Sci. Technol.* B **10** 2179
[22] Weng Y and Kushner M J 1990 *Phys. Rev.* A **42** 6192
[23] Sakabe S and Izawa Y 1992 *Phys. Rev.* A **45** 2086
[24] Leichner P K and Ericson R J 1974 *Phys. Rev.* A **9** 251
[25] McDaniel E W, Čermák V, Dalgarno A, Ferguson E E and Friedman L 1970 *Ion Molecule Reactions* (New York: Wiley-Interscience)
[26] Deloche R, Monchicourt P, Cheret M and Lambert F 1976 *Phys. Rev.* A **13** 1140
[27] Phelps A V 1955 *Phys. Rev.* **99** 1307
[28] Piper L G 1988 *J. Chem. Phys.* **88** 231
[29] Dhali S K 1989 *Trans. Plasma Sci.* **17** 603
[30] Piper L G 1987 *J. Chem. Phys.* **87** 1625
[31] Albritton D L 1978 *At. Nucl. Data Tables* **22** 1
[32] Pouvesele J M, Khacef A, Stevefelt J, Jahani H, Gylys V T and Collins C B 1988 *J. Chem. Phys.* **88** 3061
[33] Jacquin D, Bretagne J and Ferdinand R 1989 *Plasma Chem. Plasma Process* **9** 165
[34] Janev R K, Langer W D, Evans K Jr and Post D E Jr 1987 *Elementary Processes in Hydrogen–Helium Plasmas* (Berlin: Springer)